



Additive manufactured thermoplastic elastomers for low-stress driven elastocaloric cooling

Wang, Kun; Engelbrecht, Kurt; Bahl, Christian R.H.

Published in:
Applied Materials Today

Link to article, DOI:
[10.1016/j.apmt.2022.101711](https://doi.org/10.1016/j.apmt.2022.101711)

Publication date:
2023

Document Version
Publisher's PDF, also known as Version of record

[Link back to DTU Orbit](#)

Citation (APA):
Wang, K., Engelbrecht, K., & Bahl, C. R. H. (2023). Additive manufactured thermoplastic elastomers for low-stress driven elastocaloric cooling. *Applied Materials Today*, 30, Article 101711. <https://doi.org/10.1016/j.apmt.2022.101711>

General rights

Copyright and moral rights for the publications made accessible in the public portal are retained by the authors and/or other copyright owners and it is a condition of accessing publications that users recognise and abide by the legal requirements associated with these rights.

- Users may download and print one copy of any publication from the public portal for the purpose of private study or research.
- You may not further distribute the material or use it for any profit-making activity or commercial gain
- You may freely distribute the URL identifying the publication in the public portal

If you believe that this document breaches copyright please contact us providing details, and we will remove access to the work immediately and investigate your claim.



Additive manufactured thermoplastic elastomers for low-stress driven elastocaloric cooling

Kun Wang^{*}, Kurt Engelbrecht, Christian R.H. Bahl

Department of Energy Conversion and Storage, Technical University of Denmark, Anker Engelunds Vej 301, Kongens Lyngby 2800, Denmark

ARTICLE INFO

Keywords:

Elastocaloric cooling
Additive manufacturing
Elastomers
Low-stress
Strain-induced crystallization (SIC)

ABSTRACT

Exploiting the strain-induced crystallization of soft elastomeric polymers elastocaloric cooling has recently been explored as an environmental-friendly alternative to conventional refrigeration. Elastomers require a much lower applied stress to induce the elastocaloric effect compared to shape memory alloys. Several prototype coolers employing these soft polymers have been demonstrated to achieve a moderate temperature span under lower stresses. Here, we investigate the elastocaloric properties and potential cooling performance of five thermoplastic elastomers that can be 3D printed, both in the form of filaments and as Additive Manufactured (AM) parts. The materials were first characterized as filaments to screen for the elastomers with the highest elastocaloric effects. A large adiabatic temperature change of 17.8 K was obtained in the Ultimaker98A filament. AM parameters were optimized to achieve parts with satisfactory functional stability while maintaining their elastocaloric effect. As a printed part, NinjaFlex achieved a high material coefficient of performance (COP_{mat}) of 3.2 with 1.74 J/g input work at ~ 0.1 Hz, driven by a stress of 5.7 MPa. Implementing AM elastocaloric elastomers creates opportunities for the development of full-scale low-activation-stress regenerative elastocaloric cooling components that enable optimizing flow structures and enhanced heat-transfer performance.

1. Introduction

Current cooling and heating devices consume significant amounts of the electricity used worldwide and are largely dominated by conventional vapor-compression refrigeration technologies [1,2]. These technologies are based on cycles in which a refrigerant is alternately compressed and expanded to achieve a cooling cycle. Vapor compression systems can have significant environmental impact associated with leakage of their working refrigerant as well as system losses that reduce efficiency [1]. Therefore, substantial efforts have been devoted to the development of more efficient, greenhouse-gas-free refrigerants, as well as novel and alternative cooling technologies. Solid-state cooling technologies based on caloric materials, employing so-called caloric effects; (magnetocaloric [3,4], electrocaloric [5], elastocaloric [6,7], barocaloric [8]), are found to be promising, environmentally-friendly, and efficient alternatives to vapor-compression refrigeration. The caloric effects of the materials are induced by different external fields, namely a magnetic field for the magnetocaloric effect, an electric field for the electrocaloric effect, a uniaxial strain for the Elastocaloric Effect (eCE), and an isostatic pressure for the barocaloric effect.

Elastocaloric materials are attracting increasing attention and have been recommended as the most promising alternative for non-vapor-compression technology by the US Department of Energy [9]. These materials exhibit an increase in temperature when a uniaxial strain is applied and a decrease in temperature when the strain is released adiabatically. Devices based on these materials usually operate by applying a linear strain either in tension or compression to the material, but several novel driving methods such as bending and torsion have also been demonstrated [10–13]. In recent years, Shape Memory Alloys (SMAs) with an austenitic–martensitic phase transformation at room temperature have been intensively explored, among these NiTi-based SMAs [14–16], Cu-based SMAs [17,18], and NiMn-based Heusler-type magnetic SMAs [19–21]. Particularly, the NiTi-based SMAs are most commonly employed for solid-state cooling/heat-pumping system demonstration both in numerical simulation and experimental aspects [22–26]. However, driving the eCE of SMAs requires large tensile stresses as high as several hundreds of MPa, which remains a troublesome engineering challenge for practical applications [27]. For instance, commonly used Ni-Ti alloys when developed as a cooling device require large stresses reaching 1000 MPa under compression [28].

Polymer elastomers such as Natural Rubber (NR) were initially

^{*} Corresponding author.

E-mail address: kunwa@dtu.dk (K. Wang).

<https://doi.org/10.1016/j.apmt.2022.101711>

Received 12 September 2022; Received in revised form 13 November 2022; Accepted 27 November 2022

Available online 7 December 2022

2352-9407/© 2022 The Author(s). Published by Elsevier Ltd. This is an open access article under the CC BY license (<http://creativecommons.org/licenses/by/4.0/>).

Nomenclature			
<i>Abbreviations</i>			
AM	additive manufacturing	SR	solidity ratio, [-]
FFF	fused filament fabrication	ε	strain, [-]
TPU	thermoplastic polyurethane	σ	stress, [MPa]
TPPE	thermoplastic polyester	ρ	density, [kg m^{-3}]
TPEs	thermoplastic elastomers	S	entropy, [J K^{-1}]
NR	natural rubber	ω	fitting time constant, [s]
eCE	elastocaloric effect	Q	cooling/heating work, [W]
SIC	strain-induced crystallization	L	length, [m]
SMAs	shape memory alloys	m	mass, [kg]
SEM	scanning electron microscope	T	temperature, [K]
IR	infrared radiation	t	time, [s]
DSC	differential scanning calorimetry		
<i>Variables</i>		<i>Subscripts</i>	
COP	coefficient of performance, [-]	ad	adiabatic
ΔW	input work, [J]	cyc	cyclic
c_p	specific heat capacity, [$\text{J kg}^{-1} \text{K}^{-1}$]	mat	material
ΔT	temperature change	amb	ambient
		loa	loading
		unl	unloading
		c	cooling
		h	heating

reported to have elastocaloric properties by Joule in 1859, namely having the Gough-Joule effect [29]. Compared to most SMAs, the stress to trigger the eCE in the elastomers is one or two orders of magnitude less than for SMAs. Additionally, the advantages of elastomer materials include softness, low cost, sustainability, and lack of toxic materials. This has driven increasing research into exploiting various elastomers in recent years, which opens new avenues for eCE refrigeration [30–34]. The eCE in rubbers and Thermoplastic Polyurethane (TPU) elastomers has been increasingly studied and the softening effect (namely, the Mullins effect) on its caloric cooling application was elucidated as well [32,35–37]. TPU elastomers have been observed with considerable eCE at room temperature due to Strain-Induced Crystallization (SIC), which is associated with a partial crystallization of the elastomer caused by deformation [38,39]. The inherent SIC in elastomers can enhance their mechanical functionality and improve the eCE cooling performance [34, 35,40]. More recently, a novel elastocaloric cooler based on SIC using an inflating-deflating rubber membrane was developed with an attractive specific cooling power of 20.9 W/g, showing that elastomers can absorb a high cooling load per mass [34]. High cooling power has been demonstrated in vulcanized NR fibers and polyethylene wires by means of twisting, untwisting, and stretching simultaneously [12]. Thermoplastic elastomers with uniform molecular chain lengths were synthesized, and the elastocaloric effect was shown to improve [41]. These achievements in the search for eCE elastomers and in developing practical cooling prototypes based on them demonstrate the promise of regenerative elastocaloric cooling/heat-pumping systems based on elastomers.

Implementing Additive Manufacturing (AM) to engineering applications can add freedom to produce complex geometries, which has been used to develop novel regenerator structures to achieve efficient heat transfer and enhanced functional stability for solid-state cooling [42–44]. Thermoplastic Elastomers (TPEs) such as TPU, have been utilized for fabricating flexible 3D components by means of AM technologies [45,46], often using Fused Filament Fabrication (FFF). Manufacturing using FFF consists of depositing successive layers on a build plate by extruding a thermoplastic filament to obtain 3D structures. FFF is a low-cost, commercialized technology [47–50]. Commonly used AM techniques for metallic caloric materials, including selective laser melting and selective beam sintering, cannot produce smooth, fine regenerator structures and struggle to control the microstructure evolution during printing. There are also limitations in the alloy

composition, as well as the complex preparation for the raw powders [51,52]. AM of polymer TPEs is easier to implement, and precise flow channels with improved heat-transfer and flow properties are achievable using more accessible 3D printing devices.

In this work, five filaments of thermoplastic elastomers were chosen to explore their elastocaloric cooling performance. These rubber-like elastomers all exhibit some degree of eCE associated with SIC and some are shown to be promising for construction of a polymer full-scale active elastocaloric regenerator produced by additive manufacturing. We screened the possible thermoplastic elastomers in filament form and fabricated the most promising into printed parts using FFF. The main printing parameters for selected elastomeric materials and their influence on the elastocaloric cooling performance were investigated.

2. Materials and methods

2.1. Elastomeric filaments and printing parameters

Commercial 3D-printing filaments were purchased, and the materials are summarized in Supplementary Table 1. Most of them were made of thermoplastic polyurethane, except the Z-Flex filament, which was made of Thermoplastic Polyester (TPPE). The printed 3D parts (NinjaFlex, KungFu98A and Z-Flex) were printed by a Zmorph VX Printer, except the Ultimaker 95A part, which was printed by an Ultimaker S5 Pro Bundle printer. The Zmorph printer used a single extruder with a 0.3 mm nozzle and the Ultimaker S5 Pro used a 0.4 mm nozzle. The G-codes (printing instructions) were generated by Voxelizer2.0 software and Cura 4.12 for the Zmorph and Ultimaker printers, respectively. These FFF based printers deposit a 3D part layer by layer, as shown in the illustration in Fig. 1(a). The 3D-printed parts for mechanical tests and elastocaloric measurements are fabricated in dogbone shapes with the same gauge length L_0 of 15 mm and a width of 15 mm. The dogbone 3D geometry is shown in Fig. 1(a). The thicknesses of the printed dogbones are 1, 2, or 5 mm. Three bead orientations with respect to the x-axis (applied strain direction) are used to print the dogbones and marked as 0° , 45° and 90° , as shown in Fig. 1(b). The samples were printed with varying temperatures both for the extruder and build plate and travelling speeds depending on the material. The basic printing parameters for each filament, including printing temperature, bed temperature, and printing speed, are listed in Supplementary Table 1. The infill type used in FFF is line infill (or rectilinear) for all prints. Due

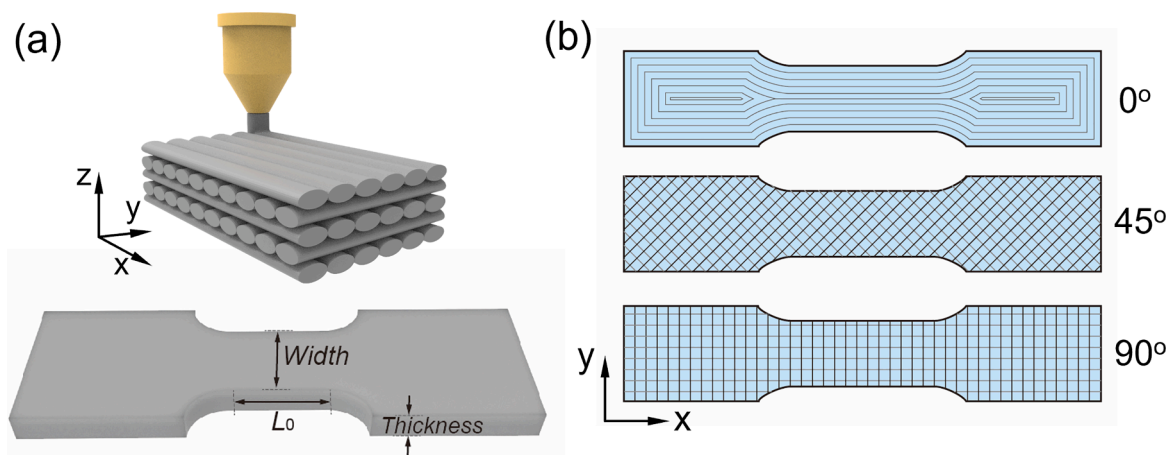


Fig. 1. FFF printing of elastomeric filaments: (a) Schematic of FFF 3D printing with cross-stacked layers and geometry of the dogbone part; (b) Three printing orientation for dogbone parts.

to the hygroscopic nature of TPU polymers [53], the filaments will absorb atmospheric moisture and during the printing the wet filament will be melted with the vapor turning to steam which leads to voids in the part and reduces mechanical properties [24]. Thus, they were stored in a filament dryer at 80 °C during and between printing in order to avoid moisture.

2.2. Mechanical tests and infrared temperature measurements for elastomers

Mechanical testing and experimental characterization of the elastocaloric effect were performed on a Zwick/Roell EZ030 electro-mechanical tester. An Xforce K load cell enabling a maximum load of 30 kN with an uncertainty of 1% was used for the tests. More detailed information regarding the mechanical tester can be obtained from the literature [34]. The printed parts and filament wires were tightly clamped by T-fatigue grips on the crosshead of the tester. Some rubber protective material was placed between the gripped area of the printed samples and the mechanical grips to protect the sample during the stretching process, which can be seen in Supplementary Fig. 1. The gauge length of 20 mm and strain rate of 5 s^{-1} are used for the filament elastocaloric measurements, where the large strain rate is implemented to achieve a quasi-adiabatic state which is comparable to the rate reported in the TPU test [36]. This fast-loading strain rate was also implemented for the quasi-adiabatic temperature change measurements in the eCE comparison of different bead orientations (the temperature change was a function of strains). The different samples were employed for different elastocaloric performance tests. Specifically, the thickness of dogbones used for the eCE comparison of different orientations was 5 mm. Dogbones applied for the stability evaluation were printed in 2 mm and the related cyclic mechanical tests were run at a strain rate of 0.33 s^{-1} and operated in a strain range of 150–500%. Dogbones employed for cyclic tests of the material COP calculation were printed with a thickness of 1 mm and the strain rate was 0.67 s^{-1} . The elastocaloric temperature change was measured using an infrared (IR) thermographic camera (InfraTec 9400). The spatial resolution and temperature resolution of the IR camera can achieve 0.01 mm/pixel and 0.02 K, respectively. In addition, due to the buckling of filaments and printed dogbones during cyclic tests and due to the large applied strains, the middle point of the sample moved during loading/unloading. Different middle zones at different states in an elastocaloric cycle were chosen from the sample to obtain the average infrared temperatures, finally combining temperature variation curves of each state into the temperature variation profile of a full cycle. For the cycling tests, a fixed selective zone for infrared temperatures was used to evaluate the adiabatic temperature change.

2.3. SEM characterization and thermal analysis

Surface microstructures of the printed parts were characterized by a Zeiss EVO MA10 Scanning Electron Microscope (SEM). The uncycled printed and cycled specimens for SEM were cut at the middle of the active region using a snap-off utility knife (BAHCO KB09-01). Before the SEM imaging, polymer specimens were processed by carbon coating on the surface to improve the conductivity. Specific heat capacity was measured on a custom built, high-resolution, Peltier element based Differential Scanning Calorimetry (DSC) [54]. The measured specimens ($\sim 0.5 \text{ mg}$) were cut from the virgin filaments, uncycled printed dogbones and 100 times cycled dogbones. The tests were performed with heating and cooling rates of 1 K/min in a vacuum of $5 \times 10^{-6} \text{ mbar}$.

3. Results & discussion

3.1. Elastocaloric properties in elastomeric filaments

Elastomeric filaments of each material were first characterized for their eCE properties and eCE cooling potential. In Fig. 2(a), a piece of NinjaFlex filament is mounted in the mechanical tester with two protective rubber gaskets surrounding both gripped ends. The temperature change and filament geometric evolution are recorded by the IR camera. Infrared thermographs present the surface temperature increase and decrease during the stretching and releasing processes (states: *ii* and *iv*, respectively), as well as the temperature equilibrium with ambient temperature $T_{\text{amb}} = 296 \text{ K}$ prior to loading and unloading (states: *i* and *iii*, respectively). In addition to the observed temperature changes, buckling occurs in state *iv* due to the plastic deformation produced by the large deformation. The time-dependent temperature evolution diagram, with the four states, is shown in Fig. 2(b), which is obtained from the average surface temperature in a selected zone from filament IR images. Notice one interesting phenomenon that the temperature increase during the loading process is higher than the decrease during the unloading process. This may be caused by some intrinsic hysteresis in the loading-unloading process (observed in the cyclic stress-strain curves in Supplementary Fig. 2). The asymmetry for temperature increases and decreases has also been observed in other rubbers and rubber-like elastomers due to the large variation of the thermal time constant and the crystallization kinetics [36,40]. Indeed, the elastic entropy and the SIC both contribute to the elastocaloric effect for natural rubbers. When the applied strain reaches 500–600% for natural rubbers, the crystallization can occur in a few tens of milliseconds upon stretching and the rubber heats up rapidly both from elastic entropy variation and the SIC process [55,56]. Upon releasing, a fraction of the crystallization will be relaxed due to the holding time in contact with the

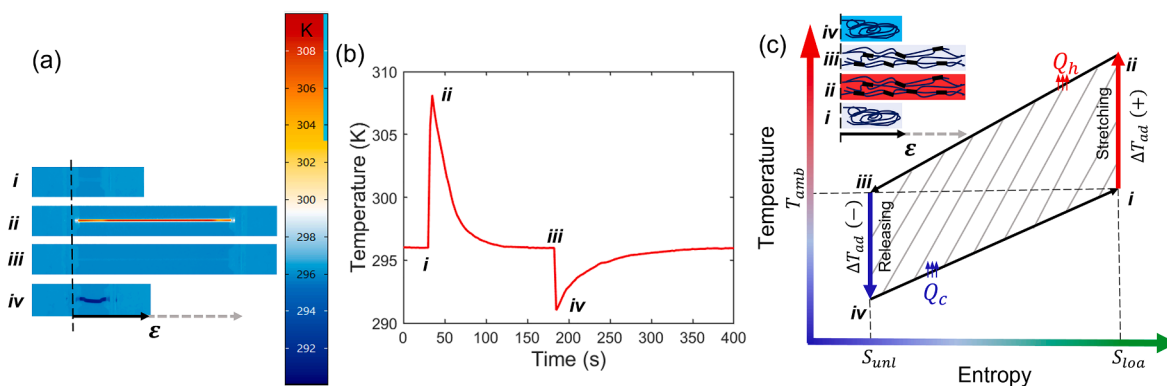


Fig. 2. Surface temperature variation for the NinjaFlex filament in an eCE cooling cycle: (a) IR images in each state of the first cycle; (b) Temperature changes of the elastocaloric material during an eCE cycle; (c) Schematic temperature-entropy diagram for an eCE cooling cycle, where (+) and (-) represent temperature increase and decrease, respectively; Q_h and Q_c represent the heating and cooling energy, respectively; The inset diagram gives a representation of the molecular chain state variation between the disordered and strain-induced crystallization (black blocks) during adiabatic stretching and releasing and the corresponding heating (red), cooling (blue), and ambient (grey) of the sample.

ambient temperature, and there is a lower contribution for the eCE from the SIC process.

An elastocaloric cooling cycle is illustrated with a temperature-entropy (T - S) diagram in Fig. 2(c) to elucidate the elastomer eCE cooling operating principle, which represents a reversed Brayton-based thermodynamic cycle. Active elastomers are subject to the four processes in the thermodynamic cycle: adiabatic stretching ($i \rightarrow ii$), fluid flow from cold to hot where heat is rejected from the hot reservoir ($ii \rightarrow iii$), adiabatic releasing ($iii \rightarrow iv$), fluid flow from hot to cold where a cooling load is absorbed in the cold reservoir ($iv \rightarrow i$). While the elastomer

undergoes the adiabatic uniaxial stretching, the applied stress leads to a partial phase transition for the elastomer molecular chains from the crimped state to the extended state. Some molecular chains crystallize into ordered phases accompanying with the latent heat and entropy increase [57]. The crystallization of elastomer molecular chains is induced by rapidly stretching, i.e., so-called strain-induced crystallization (SIC), which is the reason for the elastocaloric effect in elastomers [39,58]. The consequence is that the surface temperature increases for most of rubbers and soft elastomers. Undergoing an adiabatic releasing process, the recovery to the disordered coil-like state of SIC molecular

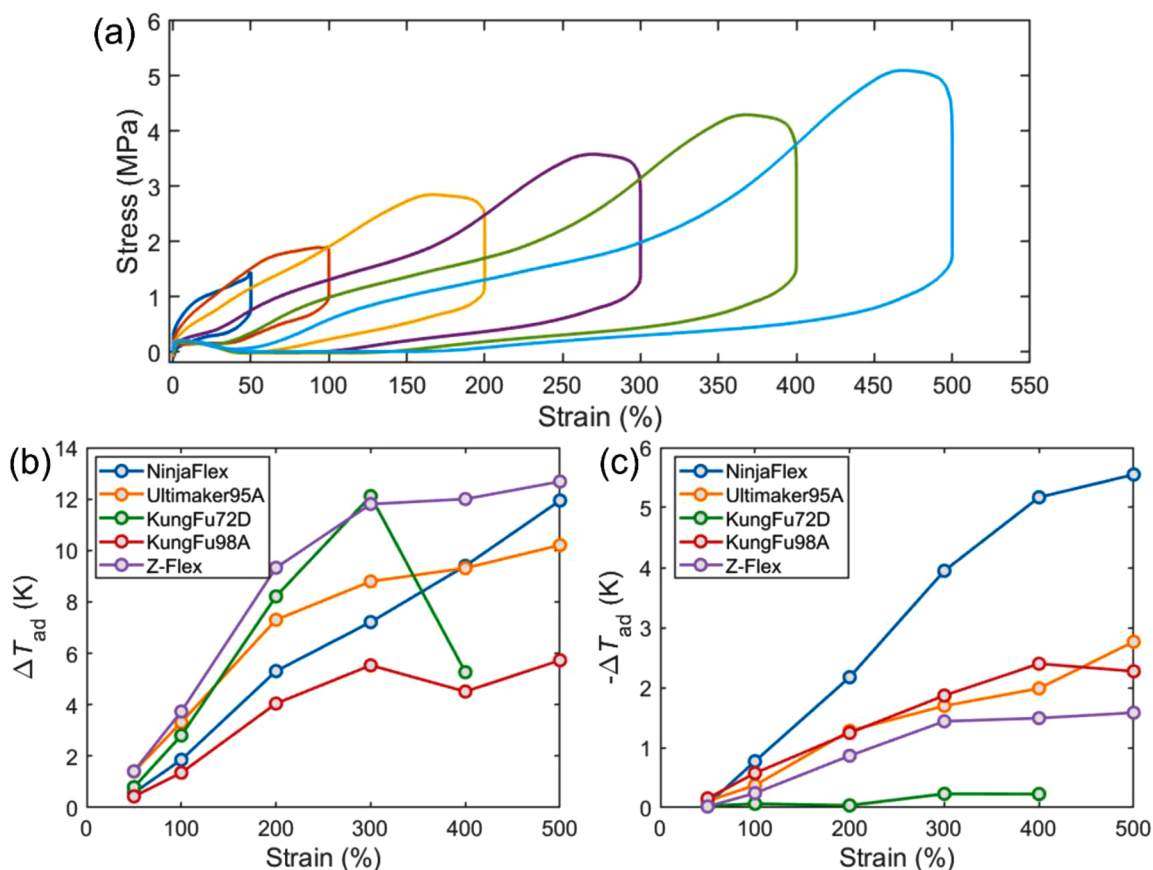


Fig. 3. Elastocaloric effect comparison for different elastomeric filaments: (a) Stress-strain profiles for the NinjaFlex filament; (b) Temperature change as a function of strain for different filaments during the filament stretching; (c) Temperature change as a function of strain for different filaments during the filament releasing.

chains leads to the absorption of heat and thus a temperature decrease.

Elastocaloric measurements for the five elastomeric filaments were performed under different strains. Fig. 3(a) shows the stress-strain behavior of the NinjaFlex filament. The measurement was performed using one filament with a sequential strain increase from 0 to 500%. The stress-strain curves and time-dependent temperatures for the other samples are given in Supplementary Figs. 3–7. The temperature changes were measured during each loading and unloading process. The system was allowed to equilibrate with ambient after each change in strain, as illustrated in the elastocaloric cycle in Fig. 2(b). Results for adiabatic temperature increases and decreases of different filaments are shown in Fig. 3(b and c). Regarding the exothermic process, the positive ΔT_{ad} gradually increases as the strain increases to 300%. Subsequently, a ΔT_{ad} plateau was observed for some samples (Ultimaker95A, KungFu98A, Z-Flex) where the adiabatic change increases very little from a strain of 300–500%. This indicates that strains above 300% for these materials are less elastocaloric responses. The adiabatic temperature change of the NinjaFlex filament continues to increase at strains above 300%, and the largest ΔT_{ad} value reaches 12 K at the strain of 500%. The endothermic process accompanying a negative ΔT_{ad} upon releasing the strain plays a significant role in evaluating the capacity for elastocaloric cooling devices. Since the KungFu72D filament failed mechanically due to its elongation between 300 and 400%, data at 400% is not available and the result for 300% may include significant plastic deformation of the sample. Furthermore, only a negligible elastocaloric effect was observed during the unloading process, which indicates that it is not an attractive material for elastocaloric cooling applications. The remaining four candidates exhibit large elastocaloric effects during the endothermic process. The negative ΔT_{ad} of the NinjaFlex filament increases with the strain increase and a maximum $-\Delta T_{ad}$ value as large as 5.55 K at 500% is achieved. The $-\Delta T_{ad}$ values for Ultimaker95A and KungFu98A filaments are similar below 500% where the adiabatic temperature changes of both are ~ 2 K. However, there is a difference in trend for the Ultimaker95A and KungFu98A filaments between the strains of 400 and 500% in Fig. 3(c). This phenomenon is similar to the behavior for the KungFu72D filament during stretching. In addition, a slight decrease in ΔT_{ad} for KungFu98A during stretching is observed in Fig. 3(b). The stress improvement (8.25%) from 2.91 to 3.15 MPa due to the strain increase from 400 to 500% is less than that (11.31%) of the Ultimaker filament from 6.01 to 6.69 MPa, (the corresponding stress-strain behavior is given in the Supplementary Figs. 4 and 6), which results in a $-\Delta T_{ad}$ drop for KungFu98A in Fig. 3(c). Although the temperature change of the Z-Flex filament was highest among these materials during the adiabatic stretching process, its $-\Delta T_{ad}$ was not as large as the value during the stretching process. A $-\Delta T_{ad}$ value of 1.58 K for the Z-Flex filament was obtained at 500% strain but a temperature change of 1.44 K was measured at 300% and thus the $-\Delta T_{ad}$ increased slightly as the strain increased to 500%.

3.2. Softening behavior and reversible elastocaloric effect

When eCE elastomeric filaments undergo several loading-unloading cycles, the stress-strain curve shows significant compliance after the first cycle and then tends towards a stabilized cycle (Supplementary Fig. 2). This softening behavior is commonly observed in rubbery materials, the so-called Mullins effect, which contributes to the elastocaloric effect decrease in natural rubbers and elastocaloric elastomers [37,46]. The eCE performance evolution associated with the softening behavior of elastomeric filaments is investigated by comparing the ΔT_{ad} ratio between the initial cycle and after a small number of cycles (~ 10). This relative variation of the adiabatic temperature is shown in Fig. 4(a) and (b) for strains of 500% and 10 cycles. The tests for each sample were conducted in three procedures: one adiabatic stretching-releasing cycle, with a pause to equilibrate with room temperature in between (initial cycle); cyclical stretching and releasing eight times (cyclic process); and one adiabatic stretching-releasing cycle with pauses for temperature equilibration (10th cycle). After the cyclic process, the values of ΔT_{ad} exhibit a significant decrease between the 1st and 10th cycles for the samples due to the irreversible plastic deformation produced during cycling [35,41]. However, the degradation of $-\Delta T_{ad}$ is smaller, and for some samples (Ultimaker, KungFu98A, and Z-Flex) the $-\Delta T_{ad}$ even increases after the cyclic process. Since the lower value of elongation at the breaking point for the KungFu72D sample, the mechanical fatigue presents after the first stretching. The highest ΔT_{ad} is produced in KungFu72D during the stretching but there is no temperature change observed during the releasing process. The lowest temperature relative variation is observed in the NinjaFlex sample both during the loading and unloading process, manifesting its reversible elastocaloric effect among these elastomeric filaments. Especially, seldom degradation in temperature change appears for NinjaFlex filament during the unloading process.

3.3. Printing orientation and its impacts on elastocaloric properties

To exploit full-scale elastocaloric regenerators printed by these potential elastomeric materials, the manufacturing parameters should be carefully examined to ensure decent elastocaloric and mechanical properties after the printing. Printing parameters such as temperatures and printing patterns can be easily controlled and are directly connected to the mechanical integrity and lifetime of the elastocaloric regenerator. For FFF, the 3D part is deposited layer by layer. Extruded beads within each layer could be aligned in different directions. The orientation of extruded beads and layers is essential to the mechanical properties of printed parts. Another parameter, solidity ratio (SR), given by the distance between beads, and thus representing the printed density, is also crucial for printing mechanical properties [59]. The highest infilled-pattern quality (95%) is applied for each printing to obtain

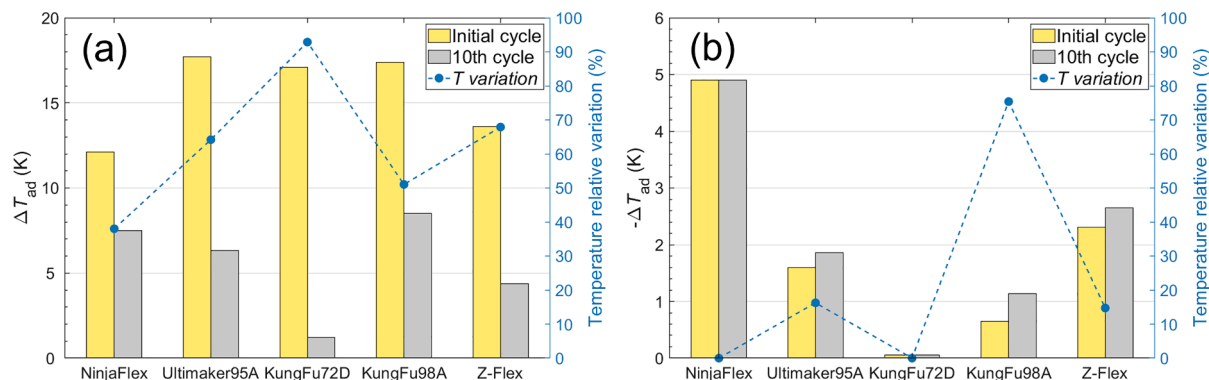


Fig. 4. Adiabatic temperature change comparison for different samples undergoing the initial cycle and 10th cycle during the stretching (a) and releasing (b) processes, and the corresponding temperature variation ratio.

samples with as high a density as possible. Therefore, the effect of the spacing between beads is not considered here. Printed parts employed for eCE cooling are subjected to uniaxial stretching, which means that stacked layers inside of the sample should be able to withstand the large cyclical uniaxial stress. Three printing profiles for the dogbone-shape parts with different orientations were chosen, as illustrated in Fig. 1 (b). In the 0° orientation the layers are stacked with the same printing pattern as the diagram shown. The dogbones with 45° and 90° orientations are printed with a cross-hatched structure in the stacked layers.

Elastocaloric effect measurements for each orientation were conducted with samples printed from the NinjaFlex filament as this was found to have the most promising properties. The surface temperature variation of the 0° dogbone undergoing the four states of an elastocaloric cycle measured by IR thermography is shown in Fig. 5(a). The temperature distribution is uniform in the middle rectangular area of the dogbone, but some higher temperatures are observed at the two ends of the active area owing to the uneven stress distribution. The measured adiabatic temperature changes during loading and unloading as a function of strain are obtained from the average temperature in the middle of the active area of each dogbone. Mechanical tests return to zero strain (the original length) at the end of every cycle. Buckling occurs due to the large deformation that occurs in stage *iv* of the dogbone test. The stress-strain behavior for the different printing orientations is compared in Fig. 5(b). The tensile modulus of differently oriented dogbones is 7.9 ± 0.6 MPa for 0° , 7.4 ± 0.8 MPa for 45° , and 6.8 ± 0.7 MPa for 90° . These are evaluated in an elastic strain range of 0–10%. The value of stress and tensile modulus decrease with an increase in orientation angle, during the loading process. This is in agreement with the results observed in various studies for FFF parts, where beads oriented parallel to the load direction (0° orientation) are always stronger than beads oriented perpendicular to the load direction [59,60]. For the 0° orientation dogbone the larger tensile modulus indicates a higher

stiffness and tighter bead attachment, and thus a denser part as well as good mechanical properties are expected. Adiabatic temperature changes during loading and unloading are shown in Fig. 5(c) and 5(d), respectively. The corresponding stress-strain curves for the elastocaloric measurements subject to different strains are given in Supplementary Fig. 8. The results of ΔT_{ad} for different dogbone orientations confirm that the 0° orientation dogbone maintains a significant elastocaloric effect in 3D printed parts. From the perspective 3D printing elastocaloric regenerators, the orientation of beads and stacked layers should be aligned parallel to the loading direction to realize the largest lifetime and eCE.

3.4. Microstructures of printed parts

The microstructures of the printed parts with different bead orientations were studied in uncycled and cycled 3D-printed parts. Fig. 6(a) and (b) show profile and cross-section views of the 0° dogbone. Good attachment between the ellipsoid beads stacked along the z-direction is achieved by the FFF printing. Interbead voids between the extruded beads are produced during the deposition process. The printed 0° dogbone was subjected to 100 cyclic tests to study the microstructural evolution after plastic deformation. From the cross-section view in Fig. 6 (c), it can be observed that the plastic deformation leads to a reduced mean width of the ellipsoid beads from $248 \pm 13 \mu\text{m}$ to $189 \pm 8 \mu\text{m}$ measured from the SEM images. Fig. 6(d and e) show the cross-section view from the 90° dogbone before stretching and after periodic stretching and releasing. The net-like connection between the extruded beads in the 90° dogbone differs from the bonding connection in the 0° dogbone, which is a parallel-stacked architecture. The size of the interbead void in the 90° uncycled dogbone is larger than that of the 0° one and the bead width decreases to $221 \pm 14 \mu\text{m}$. After deformation, the ellipsoid bead width further diminishes to $177 \pm 10 \mu\text{m}$. From Fig. 6

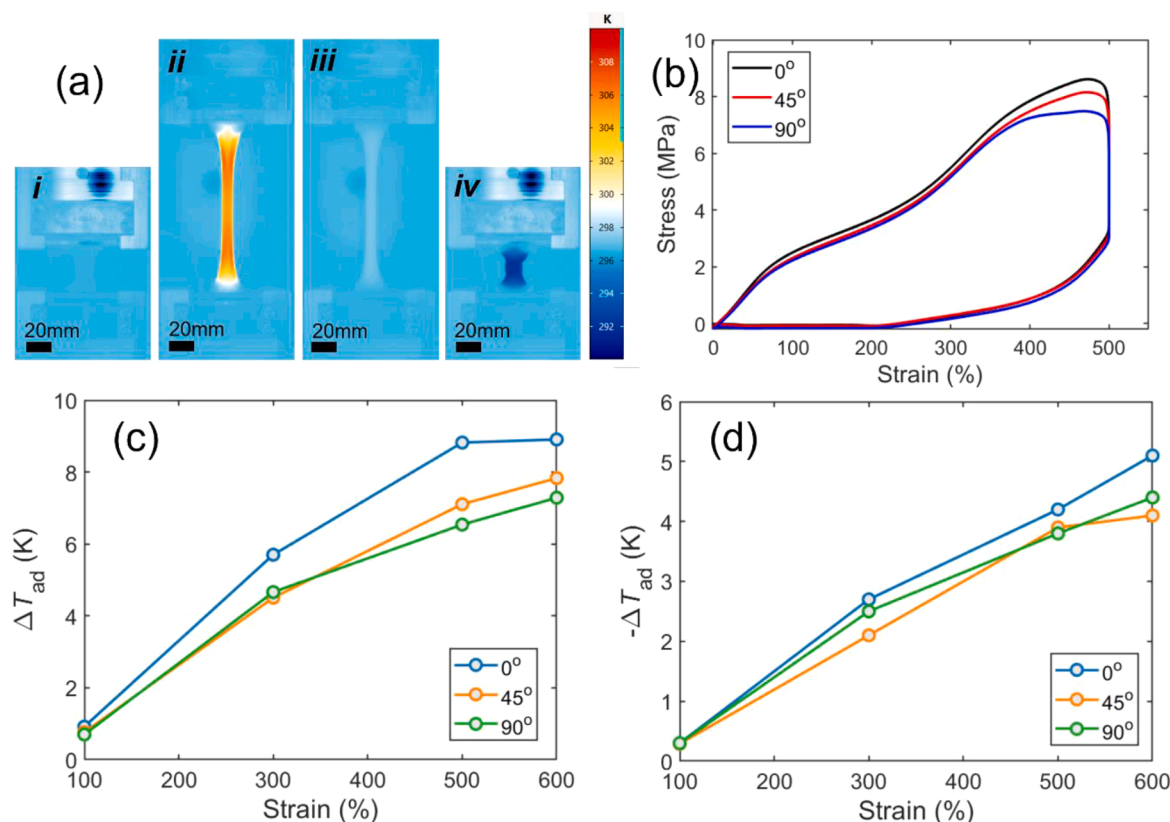


Fig. 5. Elastocaloric properties of different oriented parts: (a) IR images of printed NinjaFlex dogbone part at different states in an elastocaloric cycle; (b) Stress-strain profiles of printed NinjaFlex dogbones with different orientations; (c) Temperature change as a function of strain for different printing orientations during stretching; (d) Temperature change as a function of strain for different printing orientations during releasing.

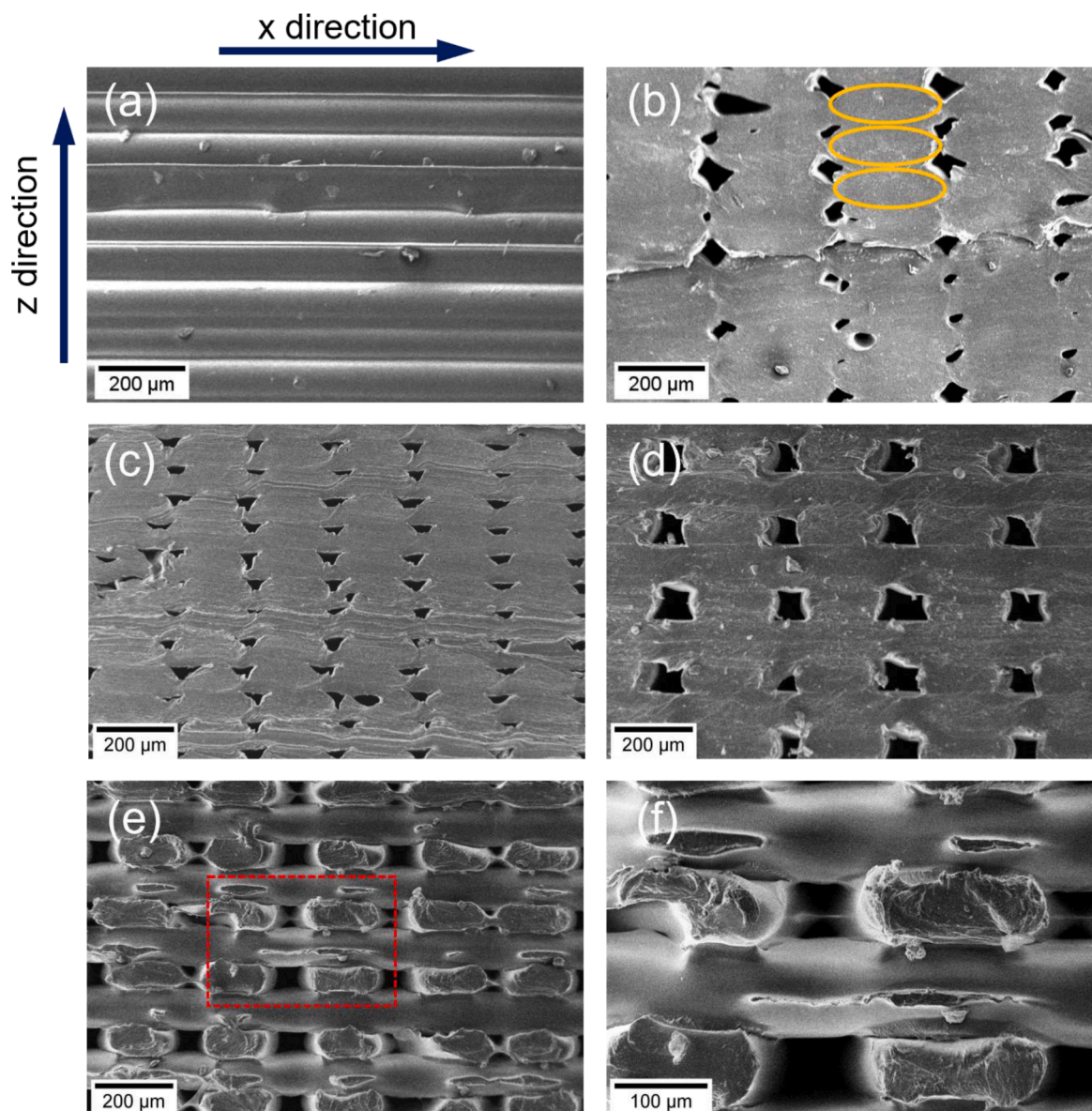


Fig. 6. Microstructures of printed parts: (a) and (b) are SEM images of the profile and cross-section views for a printed dogbone with the 0° printing orientation, respectively; (c) is a cross-section view after cycling. (d) and (e) are SEM images of profile and cross-section views for a 90° printed dogbone before and after training, respectively; (f) magnified SEM image from the red rectangular zone in (e).

(e), it can be observed that the beads parallel to the stretching direction are plastically deformed and constrained by the beads perpendicular to the stretching direction. Because the transverse beads are not subjected to the stretching, they experience no plastic deformation, which causes dimensional mismatches with the longitudinal beads that are deformed. This mismatch causes cracks on the transverse bead due to the alternating mechanical interaction between the longitudinal and transverse beads. One of the representative areas is magnified and shown in Fig. 6 (f) to accentuate the crack. It can be deduced that the mechanical interaction will also produce cracks on the longitudinal bead thereby reducing the mechanical properties of the part.

To evaluate the density of a printed FFF part quantitatively, the SR can be calculated by the area of the bead divided by the potential maximum area between the beads, indicated by a box around each bead [59]. The maximum area is determined by the layer height and the width of the bead, which is typically the nozzle diameter. A SR value of 0.79 is obtained for the printing at different orientations (calculating details are given in Supplementary Note 3). The actual normalized density is evaluated by calculating the area ratio between the solid and

pore regimes from cross-section SEM images. The values for the uncycled and cycled parts in 0° orientation are 0.97 and 0.95, respectively. For the 90° orientation one, the results are 0.93 and 0.89, respectively. All these values are higher than the theoretical value because the real bead shape is not a perfect ellipsoid and it changes during the melting and depositing process. The quantitative result for the printing density also indicates that the 0° dogbone is denser than the 90° dogbone, both before and after undergoing the cyclic loading and unloading. This is further substantiated by the higher tensile modulus obtained in the 0° dogbone. The voids caused by the 90° printing will be enlarged in the longitudinal and transverse direction during the stretching. When this part is employed in an active elastocaloric regenerator, these voids inside the regenerator can absorb the liquid heat-transfer fluid during the loading and unloading processes, resulting in parasitic heat losses. However, the voids in the 0° dogbone are disconnected, smaller, and maintain their shape under cycling. Additionally, the connection between the extruded beads in the 0° dogbone remains tight after cyclic tests. Therefore, the 0° orientation seems best for fabricating a full-scale elastocaloric regenerator, due to advantages both in elastocaloric

properties and density stability.

3.5. Stability of the mechanical and elastocaloric properties for printed elastomers

The stability of the mechanical properties and eCE of elastocaloric materials is an essential characteristic for evaluating the potential for caloric cooling applications, as it determines the lifetime of the device employing the given eCE materials. Fig. 7(a) shows 100 loading-unloading cycles for the parts printed with different orientations. Similar to the foregoing discussed on the printing orientation impacts on the eCE, the tensile modulus and the maximum stress also decreased with the printing orientation, increasing to 90° during the cyclic tests. As shown in Fig. 7(b), when increasing the cycle number, the stabilized stress can reach to 5.31 MPa for the 0° dogbone, and 3.45 MPa for the 90° dogbone. This can be explained by the higher alignment along the tensile direction for the 0° dogbone, as observed in the microstructural distribution for the extruded beads. The printed layers of the 0° dogbone maintain a good mechanical stability and therefore favor a higher uniaxial stress.

A 0° dogbone with a thickness of 2 mm is subjected to over 1000 cycles to examine the stability of the eCE and its mechanical properties. To avoid any buckling caused by the plastic deformation, the strain is set back to 150% instead of 0% during the releasing process. A slow strain rate of 0.33 s⁻¹ is applied throughout the test. The stress-strain profiles of some cycles are selected and shown in Fig. 8(a). It was observed that the maximum loading stress decreases as the cycle number increases. The temperature evolution profile of the first 85 cycles is recorded by the IR camera as shown in Fig. 8(b). After the first several cycles, the temperature variation tends to stabilize, and the detailed temperature variation for cycles 50–56 is given in Fig. 8(c). The average cyclic temperature for the 0° dogbone reaches 3.92 K. Later, the temperature profiles for cycles 955–1015 were captured, as show in Fig. 8(d). The average cyclic temperature change from cycles 1000 to 1006 is 3.09 K,

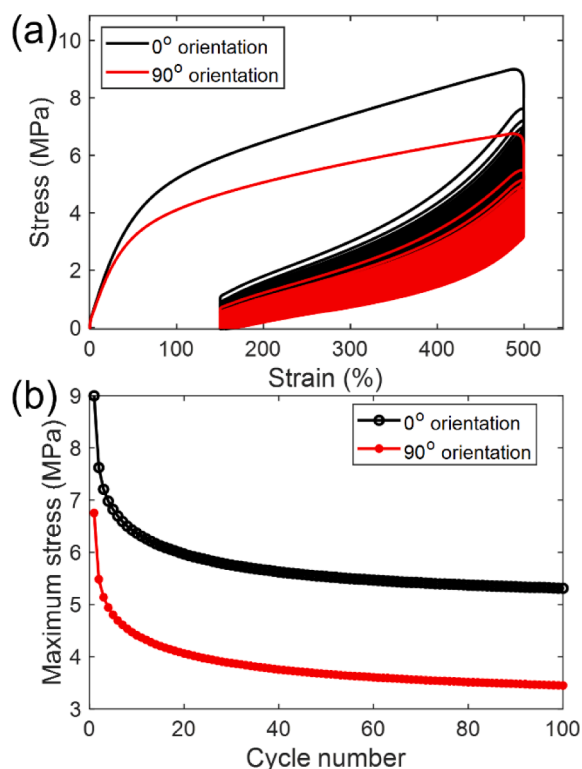


Fig. 7. (a) Stress-strain profiles of printed NinjaFlex dogbones for 100 loading-unloading cycles; (b) Evolution of the maximum stress achieved in each cycle as a function of the cycle number.

which indicates a good functional stability for the eCE of the 3D-printed NinjaFlex.

3.6. Elastocaloric cooling performance of the printed elastomers

The material coefficient of performance (COP_{mat}) is defined for evaluating and comparing potential caloric materials to be employed in caloric cooling [27]. It is calculated by the cooling energy per unit mass divided by the input work per unit mass as shown in Eq. (1). In a Brayton cycle, the cooling energy can be expressed as an integral of the specific heat capacity c_p from T_1 to T_{amb} , where the T_1 is the cold temperature obtained during the loading process and the T_{amb} is the ambient temperature. The input work is obtained from the area of the stress-strain curve. Detailed results for c_p measurements of the filament as well as the uncycled and cycled printed parts are organized and discussed in Supplementary Note 1 and Table 2.

$$COP_{mat} = \frac{Q/m}{\Delta W/m} = \frac{\int_{T_1}^{T_{amb}} c_p dT}{\frac{1}{\rho_0} \oint \sigma d\epsilon} \quad (1)$$

In practice, regenerative elastocaloric cooling will operate cyclically and the COP_{mat} calculation from the cyclic test is closer to a real elastocaloric cooling cycle. Details of COP_{mat} calculations from cyclic tests are organized in Supplementary Note 2 and Supplementary Eq. (2). Using measurements performed under near adiabatic conditions, it is found that the cyclic temperature change is dependent on the sample thickness and loading rate during cyclic tests, which is similar to the cases in active magnetic regenerators influenced by corresponding parameters such as solid thermal conductivities and operating frequencies [61,62]. Fig. 9(a and b) show the temperature change for NinjaFlex as a function of the sample thickness and loading rate. Fig. 7(a) shows that the cyclic temperature change is reduced with an increase in the thickness, due to the slow thermal diffusion from the inside to the outside. But it does not affect the temperature changes of the material under static conditions (back to room temperature after each loading and unloading process), as shown in Fig. 9(c). The difference in the temperature change in the cyclic mode is caused by convection and radiation to the ambient, which was also observed as performance differences in a rubber-based elastocaloric heat pump employing different thicknesses of polymer membranes [34]. The loading rate dependence of the temperature change, shown in Fig. 9(b), is due to the convection with the ambient. Details for loading rate impacts on cyclic temperature change are included in Supplementary Fig. 15. If the measurements are performed in an isolated environment, the temperature change will be free from the loading rate dependence which has previously been shown in some research for the elastocaloric polymers [41].

To investigate the elastocaloric properties for different sample thicknesses, samples with three different thicknesses were tested in static mode (allowing the temperature to return to room temperature after each loading and unloading process). At the same loading rate, the time to reach room temperature is longer for a thicker sample, as shown in Fig. 9(c). This can be explained by Newton's law of cooling (see, Supplementary Note 4, Supplementary Fig. 10). The heat-transfer process of surface temperature to the ambient temperature can be characterized by the time constant ω . A smaller time constant represents a faster heat transfer with the ambient. As observed in elastocaloric measurements on filaments, the temperature increases in the stretching process are higher than the temperature decreases in the releasing process for each printed part. Comparing the fitted time constant, ω , for different dogbone thicknesses, the largest values for both temperature increase and decrease are obtained with the 1 mm printed part. The fitted values of ω are 32.80 ± 0.46 s and 56.26 ± 0.29 s for cooling and heating, respectively. The time constant for the releasing process is smaller than that of the stretching process. That is because stretching will increase the heat transfer surface area of the sample. Thus, thinner samples are expected to enhance the heat transfer and thus performance

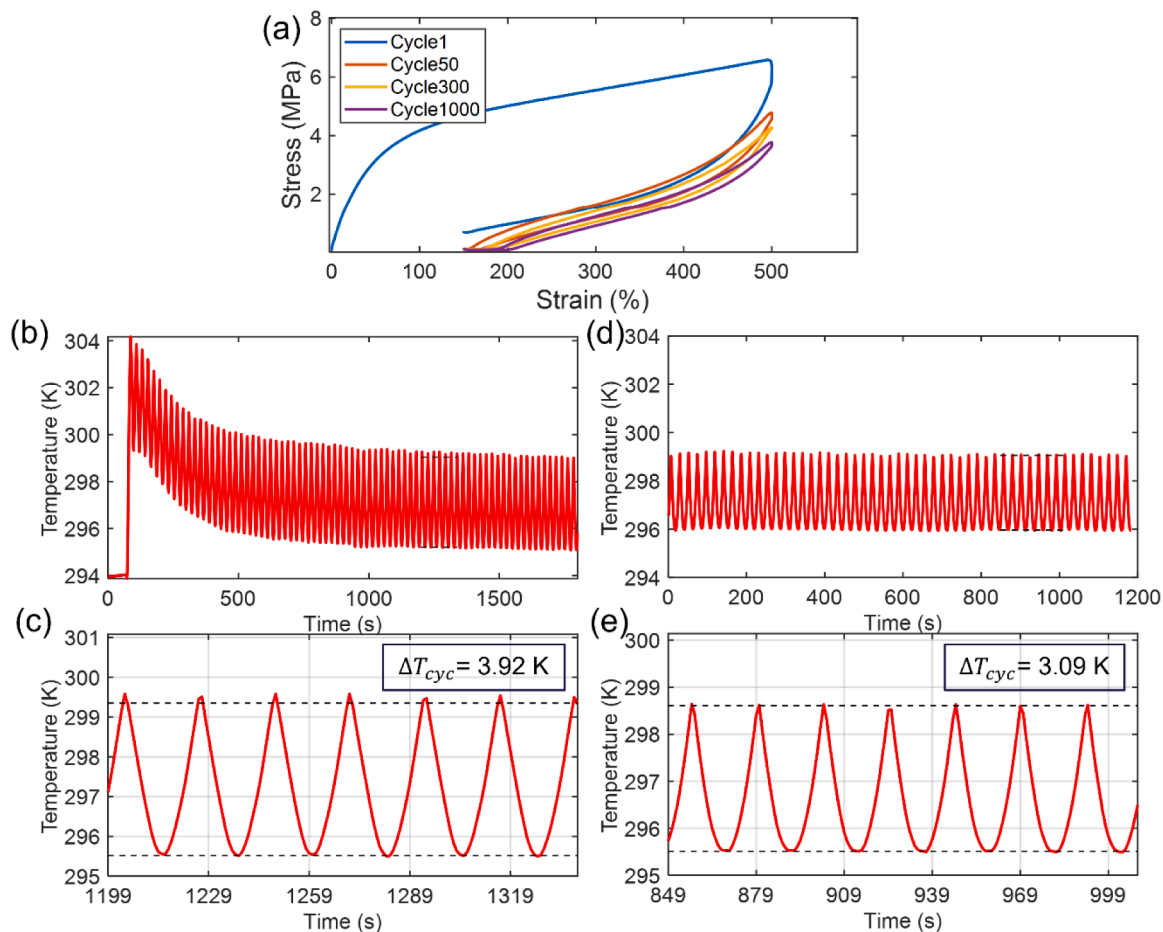


Fig. 8. Functional stability for the 2 mm printed parts over 1000 loading/unloading cycles: (a) Stress-strain behavior for the selected cycles; (b) Cyclic temperature changes for the first 85 cycles at a strain rate of 0.33 s^{-1} ; (c) Stabilized temperature change evolution in cycle numbers 50–56 selected from (b); (d) Cyclic temperature changes for cycles 955–1015 at a strain rate of 0.33 s^{-1} ; (e) Stabilized temperature change evolution in cycle numbers 1000–1006 selected from (d).

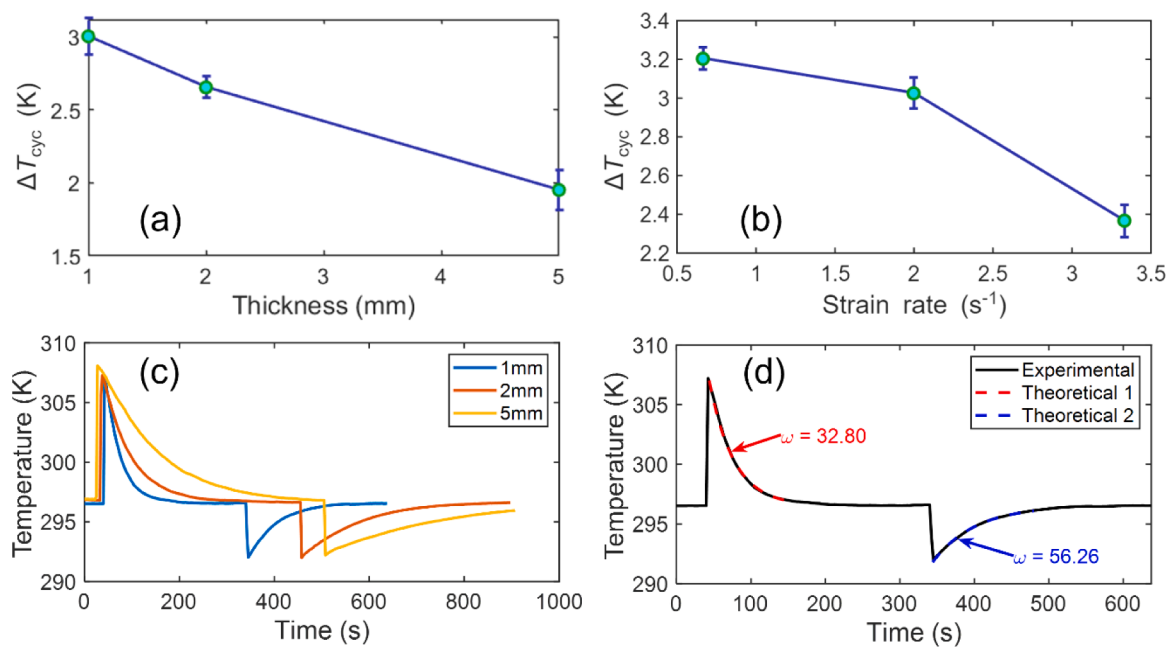


Fig. 9. Temperature variation comparison for different conditions in NinjaFlex 0° dogbones: (a) Cyclic adiabatic temperature changes for different thicknesses at a 2 s^{-1} strain rate; (b) Cyclic adiabatic temperature changes for 1 mm dogbones under different loading rates; (c) Surface temperature variation to ambient temperature by natural convection for different thickness dogbones; (d) Fits to the surface temperature versus time curves of the 1 mm dogbone.

for eCE elastomers.

Fig. 10(a) shows the cyclic temperature variation in a stable loading-unloading state. The adiabatic temperature change for the cyclic mode is defined as the distance between the top and bottom peaks during loading and unloading. When the loading-unloading process reaches cyclical steady state, the adiabatic temperature change will be stable and remains constant for the following cycles, reflecting its prominent and stabilized cycling performance. The ΔT_{cyc} for different materials during cycles 60–100 are shown in Fig. 10(b). The 0° NinjaFlex dogbone produces the largest average ΔT_{cyc} value of 3.24 K during these 40 cycles. However, we noticed that the ΔT_{cyc} for the 1 mm dogbone is less than the ΔT_{cyc} of 3.92 K obtained for the 2 mm NinjaFlex dogbone in Section 3.5. That is because the cyclic test in the stability evaluation is operated at a much lower strain rate, which would favor a higher temperature change as the results shown in Fig. 9(b). The temperature change for the Z-Flex sample is also able to reach a considerable value of 2.84 K. COP_{mat} and the input work (ΔW) as a function of the cycle number for the NinjaFlex Ultimaker95A, KungFu98A, Z-Flex materials rapidly increase during the first ten cycles and tend to stabilize in the following cycles, seeing Fig. 10(c) for NinjaFlex and Supplementary Fig. 16 for other materials. The temperature changes and the input work per unit mass in each cycle for different materials are obtained from temperature profiles given in the Supplementary Fig. 17 which exhibit a rapid decrease over the first several cycles, ending in a stable state. The average COP_{mat} and input work per unit mass during the stabilized cycles (80–100th) for different materials are compared in Fig. 10(d). The highest COP_{mat} of 3.14 with 1.74 J/g input work is observed in the NinjaFlex part at an operating frequency of ~ 0.1 Hz. From the stress-strain behavior of the Z-Flex printed part (Supplementary Fig. 14), it can be noticed that the input work is significantly reduced as the number of cycles is increased (among proposed materials the lowest input work of 1.63 J/g is required). Therefore, a considerable COP_{mat} of 3.04 with an input work of 1.63 J/g for Z-Flex is obtained when cycling 100 times despite its small temperature change.

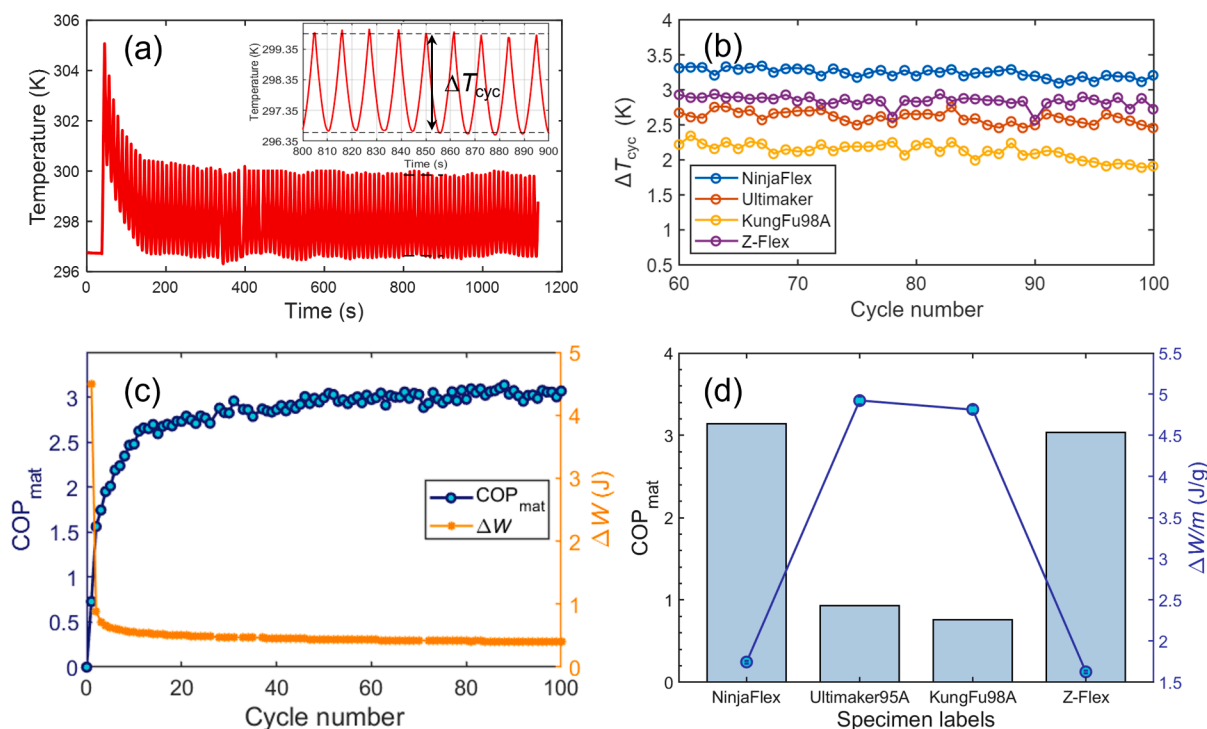


Fig. 10. Cyclic temperature characteristics and material COP_{mat} for different elastomers: (a) Time-dependent surface temperature for cyclic tests and the detailed temperature oscillation of a NinjaFlex 0° dogbone stretched at 500% strain and 0.67 s^{-1} strain rate; (b) Stabilized temperature change evolution in cycle numbers 60–100 for different materials; (c) COP_{mat} and input work evolution as a function of the number of cycles for NinjaFlex dogbone; (d) Average COP_{mat} and input work per unit mass during cycles 80–100 for different materials as printed parts in 0° orientation.

The comparison of the COP_{mat} for some common elastocaloric SMAs and polymers is summarized in the Table 1. Compared to the commonly used SMAs materials, the studied 3D printed NinjaFlex and Z-Flex polymer elastomers are superior in considerably lower driving stress (~ 6 MPa, 500%) and provide a desirable elastocaloric performance. It can be observed that the cyclic temperature change for the NinjaFlex reaches 3.92 K which is lower than several Ni-Ti alloys but comparable to the ΔT_{cyc} of 4.6 K for the $\text{Cu}_{68.3}\text{Al}_{27.1}\text{Ni}_{4.6}$ SMA. There are some differences in the material COP calculation presented in literature. For the shape memory alloys, the COP_{mat} are obtained with a correction for the irreversibility of the phase transformation process [63]. For rubber-like materials due to less hysteresis, Eq. (1) was used for the COP_{mat} calculation [36,41]. Here the NinjaFlex, Ultimaker 95A, and KungFu 98A filaments both consist of the thermoplastic polyurethane, but there are differences in the elastocaloric effect and COP_{mat} when comparing to the reported elastocaloric TPU [36]. That results from different types of TPU being used and a maximum temperature change employed for the COP_{mat} calculations in literature.

3.7. Prospects for an operation system for large deformation eCE regenerators

Compared to the experimental system for elastocaloric cooling/heat pumping using SMAs, soft elastomeric eCE regenerators require much larger deformations (300–500%) to achieve a considerable eCE. At present, some related elastocaloric coolers based on the elastomers have been designed by inflation/deflation devices or by rolling onto a rotational wheel to trigger the eCE of polymer elastomers subjected to a large deformation [34,41]. These designs give inspiration to apply the elastomeric eCE polymers in the solid-state cooling/heat-pumping field. However, when considering the construction of an experimental active elastocaloric cooling/heat-pumping system for polymer elastomers, the large deformation raises several issues, including buckling, and fluid-channel volume change. It can be predicted that the fluid-channel

Table 1

Comparison of reported elastocaloric materials on the maximum absolute adiabatic temperature change ($|\Delta T_{ad}|$) achieved, adiabatic cyclic temperature change (ΔT_{cyc}), driving stress, strains, and COP_{mat} .

Materials	$ \Delta T_{ad} $ (K)	ΔT_{cyc} (K)	$\Delta\sigma$ (MPa)	ϵ (%)	COP_{mat}	Refs.
NinjaFlex	12	3.24–3.92	5.7	500	3.14	
Ultimaker95A	17.8	2.84	11.7	500	0.93	This work
KungFu98A	17.2	2.62	11.3	500	0.76	
Z-Flex	13.5	2.28	6.4	500	3.04	
Ni-Ti	22	10–29	800	5	7.5	[64–66]
(Ni ₅₀ Mn _{31.5} Ti _{18.5}) _{99.8} B _{0.2}	31.5	–	700	7	–	[19]
Cu _{68.3} Al _{27.1} Ni _{4.6}	13.6	4.6	400	7.5	9.5	[67]
Cu _{68.2} Zn _{15.7} Al _{16.1}	15.3	–	118	8	10.6	[68]
Ni _{50.0} Fe _{19.0} Ga _{27.1} Co _{3.9}	11	7.2	130	3.8	4 (system)	[69]
NR	3.5–12	2	1–4.2	600–800	2.08	[32,37,55]
Synthetic rubbers	1.7–2.1	–	5.8–10	300–600	0.23–0.3	[37]
SEBS	15.3	–	12	600	16.2	[41]
TPU	8	3.3–4.5	6.5	400	8	[36]

–: did not find.

volume inside the 3D-printed eCE regenerator changes when the regenerator undergoes a larger deformation due to the Poisson's ratio and strain-induced material volume change [70–73]. The fluid channel volume is expected to increase during the stretching process and decrease during the releasing process, which will lead to asymmetric fluid-flow volumes between the hot/cold blows. Therefore, operating a large deformation regenerator in a flow system, the empty volume from the stretching process needs to be compensated by the flow system. On the other hand, the compensated fluid from the stretching process should be expelled back to the flow system during the releasing process, otherwise, the extra fluid can increase the pressure and may cause leakage. Future work could include a tailored fluid network configuration and operation strategy capable of handling the change of fluid channel volume in an elastomeric regenerator.

4. Conclusion

We explored the elastocaloric cooling performance of five thermo-plastic elastomers and demonstrated the potential for fabricating the soft elastomers directly into full-scale elastocaloric regenerators via additive manufacturing technologies. The elastocaloric effect in the five elastomeric filaments were initially investigated before manufacturing the filaments into 3D parts using FFF. Except for KungFu72D, the studied filaments show a satisfactory reversible elastocaloric effect. We found that the 3D-printed parts with the extruded beads aligned in parallel to the uniaxial strain direction can achieve an elastocaloric effect similar to the raw filament with stable mechanical behavior. NinjaFlex and Z-Flex dogbones exhibited a COP_{mat} of 3.14 and 3.04, respectively, at a low required stress of ~ 6 MPa, which makes them potentially attractive for elastocaloric devices. Combining AM technologies with printable elastocaloric elastomer can result in full-scale elastocaloric regenerator that can be printed directly and actuated at significantly lower forces than comparable SMA systems.

Several challenges need to be overcome for AM elastocaloric regenerator systems to achieve high performance. Since the heat-transfer fluid will flow through internal channels inside the regenerator, the AM parameters should be optimized to achieve fine regenerator geometries as well as being watertight. These would improve the fluid channel quality that could lower the flow pressure drop and enhance the heat-transfer performance. Another challenge is the large elongation required to achieve a high eCE for elastomeric regenerators, which will require special design of external equipment. There are also a number of issues that stem from the large required strains, including: softening behavior (Mullins effect), which occurs during the first cycle, and buckling during strain release caused by plastic deformation, which will bend/twist the fluid channels and influence the heat exchange. A certain number of training cycles until reaching the stable behavior could be a solution for the softening issue of these soft elastomers. Similar to the

suggested pre-elongation method implemented in natural rubbers [35], the buckling can be avoided by applying the pre-strain approach, performed by unloading to a given strain. Additionally, manipulating the pre-elongation to the eve of SIC enables higher efficient elastocaloric cooling resulting from less mechanical energy input. Overall, these achievements show a great potential to construct the soft active elastocaloric regenerator with distinct low-driven stress, opening the opportunity to develop high-performance elastocaloric cooling regenerators with optimized heat-transfer properties and structures by means of additive manufacturing.

CRediT authorship contribution statement

Kun Wang: Conceptualization, Methodology, Investigation, Validation, Data curation, Formal analysis, Visualization, Writing – original draft, Project administration. **Kurt Engelbrecht:** Supervision, Writing – review & editing, Formal analysis, Funding acquisition. **Christian R.H. Bahl:** Supervision, Writing – review & editing, Formal analysis, Funding acquisition.

Declaration of Competing Interest

The authors declare that they have no known competing financial interests or personal relationships that could have appeared to influence the work reported in this paper.

Data availability

The data that has been used is confidential.

Acknowledgments

K. Wang is grateful for financial support of the China Scholarship Council (CSC, No. 202004910369) scholarship. We wish to acknowledge Dr. Lucia Ianniciello for the help in the mechanical and IR tests.

Supplementary materials

Supplementary material associated with this article can be found, in the online version, at doi:10.1016/j.apmt.2022.101711.

References

- [1] L.W. Davis, P.J. Gertler, Contribution of air conditioning adoption to future energy use under global warming, Proc. Natl. Acad. Sci 112 (2015) 5962–5967, <https://doi.org/10.1073/PNAS.1423558112>.
- [2] J.L. Dupont, P. Domanski, P. Lebrun, The role of refrigeration in the global economy 38th note on refrigeration technologies, Int. Inst. Refrig. (2019).

- [3] V.K. Pecharsky, K.A. Gschneidner, Giant magnetocaloric effect in $Gd_5(Si_2Ge_2)$, *Phys. Rev. Lett.* 78 (1997) 4494–4497, <https://doi.org/10.1103/PhysRevLett.78.4494>.
- [4] V.K. Pecharsky, K.A. Gschneidner, Magnetocaloric effect and magnetic refrigeration, *J. Magn. Magn. Mater.* 200 (1999) 44–56, [https://doi.org/10.1016/S0304-8853\(99\)00397-2](https://doi.org/10.1016/S0304-8853(99)00397-2).
- [5] B. Neese, B.J. Chu, S.G. Lu, Y. Wang, E. Furman, Q.M. Zhang, Large electrocaloric effect in ferroelectric polymers near room temperature, *Science* 321 (2008) 821–823, <https://doi.org/10.1126/science.1159655>.
- [6] T. Krenke, E. Duman, M. Acet, E.F. Wassermann, X. Moya, L. Manosa, A. Planes, Inverse magnetocaloric effect in ferromagnetic Ni-Mn-Sn alloys, *Nat. Mater.* 4 (2005) 450–454, <https://doi.org/10.1038/nmat1395>.
- [7] J. Tušek, K. Engelbrecht, R. Millán-Solsona, L. Mañosa, E. Vives, L.P. Mikkelsen, N. Pryds, The elastocaloric effect: a way to cool efficiently, *Adv. Energy Mater.* 5 (2015) 1–5, <https://doi.org/10.1002/aenm.201500361>.
- [8] B. Li, Y. Kawakita, S. Ohira-Kawamura, T. Sugahara, H. Wang, J. Wang, Y. Chen, S. I. Kawaguchi, S. Kawaguchi, K. Ohara, K. Li, D. Yu, R. Mole, T. Hattori, T. Kikuchi, S.I. Yano, Z. Zhang, Z. Zhang, W. Ren, S. Lin, O. Sakata, K. Nakajima, Z. Zhang, Colossal barocaloric effects in plastic crystals, *Nature* 567 (2019) 506–510, <https://doi.org/10.1038/s41586-019-1042-5>.
- [9] US Department of Energy, Energy Savings Potential and RD&D Opportunities for Non-Vapor-Compression HVAC Technologies, US Department Energy, 2014, p. 199. <http://www.osti.gov/home/%0Ahttp://www.osti.gov/servlets/purl/1220817/>.
- [10] X. Moya, S. Kar-Narayan, N.D. Mathur, Caloric materials near ferroic phase transitions, *Nat. Mater.* 13 (2014) 439–450, <https://doi.org/10.1038/nmat3951>.
- [11] L. Mañosa, A. Planes, Materials with giant mechanocaloric effects: cooling by strength, *Adv. Mater.* 29 (2017), <https://doi.org/10.1002/adma.201603607>.
- [12] R. Wang, S.L. Fang, Y.C. Xiao, E.L. Gao, N. Jiang, Y.W. Li, L.L. Mou, Y.N. Shen, W. Bin Zhao, S.T. Li, A.F. Fonseca, D.S. Galvão, M. Chen, W.Q. He, K.Q. Yu, H. B. Lu, X.M. Wang, D. Qian, A.E. Aliev, N. Li, C.S. Haines, Z.S. Liu, J. Mu, Z. Wang, S.G. Yin, M.D. Lima, B. An, X. Zhou, Z.F. Liu, R.H. Baughman, Torsional refrigeration by twisted, coiled, and supercoiled fibers, *Science* 366 (2019) 216–221, <https://doi.org/10.1126/science.aax6182>.
- [13] A. Czernuszewicz, L. Griffith, J. Slaughter, V. Pecharsky, Low-force compressive and tensile actuation for elastocaloric heat pumps, *Appl. Mater. Today* 19 (2020), 100557, <https://doi.org/10.1016/j.apmt.2020.100557>.
- [14] J. Cui, Y. Wu, J. Muehlbauer, Y. Hwang, R. Radermacher, S. Fackler, M. Wuttig, I. Takeuchi, Demonstration of high efficiency elastocaloric cooling with large Δt using NiTi wires, *Appl. Phys. Lett.* 101 (2012) 2–6, <https://doi.org/10.1063/1.4746257>.
- [15] G.J. Pataky, E. Ertekin, H. Sehitoglu, Elastocaloric cooling potential of NiTi, Ni_2FeGa , and $CoNiAl$, *Acta Mater.* 96 (2015) 420–427, <https://doi.org/10.1016/j.actamat.2015.06.011>.
- [16] J. Tušek, K. Engelbrecht, L.P. Mikkelsen, N. Pryds, Elastocaloric effect of Ni-Ti wire for application in a cooling device, *J. Appl. Phys.* 117 (2015), <https://doi.org/10.1063/1.4913878>.
- [17] E. Bonnot, R. Romero, L. Mañosa, E. Vives, A. Planes, Elastocaloric effect associated with the martensitic transition in shape-memory alloys, *Phys. Rev. Lett.* 100 (2008) 1–4, <https://doi.org/10.1103/PhysRevLett.100.125901>.
- [18] L. Iannicello, M. Romanini, L. Mañosa, A. Planes, K. Engelbrecht, E. Vives, Tracking the dynamics of power sources and sinks during the martensitic transformation of a Cu-Al-Ni single crystal, *Appl. Phys. Lett.* 116 (2020), <https://doi.org/10.1063/5.0006859>.
- [19] D. Cong, W. Xiong, A. Planes, Y. Ren, L. Mañosa, P. Cao, Z. Nie, X. Sun, Z. Yang, X. Hong, Y. Wang, Colossal elastocaloric effect in ferroelastic Ni-Mn-Ti alloys, *Phys. Rev. Lett.* 122 (2019), 255703, <https://doi.org/10.1103/PhysRevLett.122.255703>.
- [20] J. Liu, T. Gottschall, K.P. Skokov, J.D. Moore, O. Gutfleisch, Giant magnetocaloric effect driven by structural transitions, *Nat. Mater.* 11 (2012) 620–626, <https://doi.org/10.1038/nmat3334>.
- [21] W. Sun, J. Liu, D. Zhao, M. Zhang, Directional solidification and elastocaloric effect in a $Ni_{45}Mn_{44}Sn_{11}$ magnetic shape memory alloy, *J. Phys. D: Appl. Phys.* 50 (2017), <https://doi.org/10.1088/1361-6463/aa87ef>.
- [22] J. Tušek, K. Engelbrecht, D. Eriksen, S. Dall'Olivo, J.J. Tušek, N. Pryds, A regenerative elastocaloric heat pump, *Nat. Energy* 1 (2016) 1–6, <https://doi.org/10.1038/nenergy.2016.134>.
- [23] S. Qian, L. Yuan, J. Yu, G. Yan, Numerical modeling of an active elastocaloric regenerator refrigerator with phase transformation kinetics and the matching principle for materials selection, *Energy* 141 (2017) 744–756, <https://doi.org/10.1016/j.energy.2017.09.116>.
- [24] V.M. Bruère, A. Lion, J. Holtmannspötter, M. Jöhltz, Under-extrusion challenges for elastic filaments: the influence of moisture on additive manufacturing, *Prog. Addit. Manuf.* 7 (2022) 445–452, <https://doi.org/10.1007/s40964-022-00300-y>.
- [25] L. Yuan, Y. Wang, J. Yu, A. Greco, C. Masselli, S. Qian, Numerical study of a double-effect elastocaloric cooling system powered by low-grade heat, *Appl. Therm. Eng.* 218 (2023), 119302, <https://doi.org/10.1016/j.applthermaleng.2022.119302>.
- [26] C. Aprea, A. Greco, A. Maiorino, C. Masselli, The employment of caloric-effect materials for solid-state heat pumping, *Int. J. Refrig.* 109 (2020) 1–11, <https://doi.org/10.1016/j.jrefrig.2019.09.011>.
- [27] S. Qian, Y. Geng, Y. Wang, J. Ling, Y. Hwang, R. Radermacher, I. Takeuchi, J. Cui, A review of elastocaloric cooling: Materials, cycles and system integrations, *Int. J. Refrig.* 64 (2016) 1–19, <https://doi.org/10.1016/j.jrefrig.2015.12.001>.
- [28] L. Iannicello, K. Bartholomé, A. Fitger, K. Engelbrecht, Long life elastocaloric regenerator operating under compression, *Appl. Therm. Eng.* 202 (2022), 117838, <https://doi.org/10.1016/j.applthermaleng.2021.117838>.
- [29] J.P. Joule, On some thermo-dynamic properties of solids, *Philos. Trans.* 149 (1859).
- [30] H.J. Qi, M.C. Boyce, Stress-strain behavior of thermoplastic polyurethanes, *Mech. Mater.* 37 (2005) 817–839, <https://doi.org/10.1016/j.mechmat.2004.08.001>.
- [31] T. Sui, N. Baimpas, I.P. Dolbnya, C. Priscacariu, A.M. Korsunsky, Multiple-length-scale deformation analysis in a thermoplastic polyurethane, *Nat. Commun.* 6 (2015) 1–9, <https://doi.org/10.1038/ncomms7583>.
- [32] D. Guyomar, Y. Li, G. Sebald, P.J. Cottinet, B. Ducharme, J.F. Capsal, Elastocaloric modeling of natural rubber, *Appl. Therm. Eng.* 57 (2013) 33–38, <https://doi.org/10.1016/j.applthermaleng.2013.03.032>.
- [33] Y. Yoshida, K. Yuse, D. Guyomar, J.F. Capsal, G. Sebald, Elastocaloric effect in poly(vinylidene fluoride-trifluoroethylene-chlorotrifluoroethylene) terpolymer, *Appl. Phys. Lett.* 108 (2016), 242904, <https://doi.org/10.1063/1.4953770>.
- [34] F. Greibich, R. Schwödiauer, G. Mao, D. Wirthl, M. Drack, R. Baumgartner, A. Kogler, J. Stadlbauer, S. Bauer, N. Arnold, M. Kaltenbrunner, Elastocaloric heat pump with specific cooling power of 20.9 W g⁻¹ exploiting snap-through instability and strain-induced crystallization, *Nat. Energy* 6 (2021) 260–267, <https://doi.org/10.1038/s41560-020-00770-w>.
- [35] Z. Xie, G. Sebald, D. Guyomar, Elastocaloric effect dependence on pre-elongation in natural rubber, *Appl. Phys. Lett.* 107 (2015), 081905, <https://doi.org/10.1063/1.4929395>.
- [36] G. Coativy, H. Haissoune, L. Seveyrat, G. Sebald, L. Chazeau, J.M. Chenal, L. Lebrun, Elastocaloric properties of thermoplastic polyurethane, *Appl. Phys. Lett.* 117 (2020), 193903, <https://doi.org/10.1063/5.0023520>.
- [37] R. Bennacer, B. Liu, M. Yang, A. Chen, Refrigeration performance and the elastocaloric effect in natural and synthetic rubbers, *Appl. Therm. Eng.* 204 (2021), 117938, <https://doi.org/10.1016/j.applthermaleng.2021.117938>.
- [38] S.L. Dart, E. Guth, Rise of temperature on fast stretching of butyl rubber, *J. Chem. Phys.* 13 (1945) 28–36, <https://doi.org/10.1063/1.1723964>.
- [39] M. Tosaka, Strain-induced crystallization of crosslinked natural rubber as revealed by X-ray diffraction using synchrotron radiation, *Polym. J.* 39 (2007) 1207–1220, <https://doi.org/10.1295/polymj.PJ2007059>.
- [40] Z. Xie, G. Sebald, D. Guyomar, Comparison of direct and indirect measurement of the elastocaloric effect in natural rubber, *Appl. Phys. Lett.* 108 (2016), 041901, <https://doi.org/10.1063/1.4940378>.
- [41] S. Zhang, Q. Yang, C. Li, Y. Fu, H. Zhang, Z. Ye, X. Zhou, Q. Li, T. Wang, S. Wang, W. Zhang, C. Xiong, Q. Wang, Solid-state cooling by elastocaloric polymer with uniform chain-lengths, *Nat. Commun.* 13 (2022) 1–7, <https://doi.org/10.1038/s41467-021-27746-y>.
- [42] H. Hou, E. Simsek, T. Ma, N.S. Johnson, S. Qian, C. Cissé, D. Stasak, N. Al Hasan, L. Zhou, Y. Hwang, R. Radermacher, V.I. Levitas, M.J. Kramer, M.A. Zaeem, A. P. Stebner, R.T. Ott, J. Cui, I. Takeuchi, Fatigue-resistant high-performance elastocaloric materials made by additive manufacturing, *Science* 366 (2019) 1116–1121, <https://doi.org/10.1126/science.aax7616>.
- [43] K. Navickaitė, J. Liang, C. Bahl, S. Wieland, T. Buchenau, K. Engelbrecht, Experimental characterization of active magnetic regenerators constructed using laser beam melting technique, *Appl. Therm. Eng.* 174 (2020) 1–12, <https://doi.org/10.1016/j.applthermaleng.2020.115297>.
- [44] E. Stevens, K. Kimes, D. Salazar, A. Mostafaei, R. Rodriguez, A. Acierio, P. Lázpita, V. Chernenko, M. Chmielus, Mastering a 1.2 K hysteresis for martensitic paraferromagnetic partial transformation in Ni-Mn(Cu)-Ga magnetocaloric material via binder jet 3D printing, *Addit. Manuf.* 37 (2021), <https://doi.org/10.1016/j.addma.2020.101560>.
- [45] A.D. Valentine, T.A. Busbee, J.W. Boley, J.R. Raney, A. Chortos, A. Kotikian, J. D. Berrigan, M.F. Durstock, J.A. Lewis, Hybrid 3D printing of soft electronics, *Adv. Mater.* 29 (2017) 1–8, <https://doi.org/10.1002/adma.201703817>.
- [46] R. Adams, S.P. Soe, R. Santiago, M. Robinson, B. Hanna, G. McShane, M. Alves, R. Burek, P. Theobald, A novel pathway for efficient characterisation of additively manufactured thermoplastic elastomers, *Mater. Des.* 180 (2019), 107917, <https://doi.org/10.1016/j.matdes.2019.107917>.
- [47] N.G. Tanikella, B. Wittbrodt, J.M. Pearce, Tensile strength of commercial polymer materials for fused filament fabrication 3D printing, *Addit. Manuf.* 15 (2017) 40–47, <https://doi.org/10.1016/j.addma.2017.03.005>.
- [48] C. Oztan, S. Ballikaya, U. Ozgun, R. Karkkainen, E. Celik, Additive manufacturing of thermoelectric materials via fused filament fabrication, *Appl. Mater. Today* 15 (2019) 77–82, <https://doi.org/10.1016/j.apmt.2019.01.001>.
- [49] X. Gao, S. Qi, X. Kuang, Y. Su, J. Li, D. Wang, Fused filament fabrication of polymer materials: a review of interlayer bond, *Addit. Manuf.* 37 (2021), 101658, <https://doi.org/10.1016/j.addma.2020.101658>.
- [50] D. Fico, D. Rizzo, R. Casciaro, C.E. Corcione, A review of polymer-based materials for fused filament fabrication (FFF): focus on sustainability and recycled materials, *Polymers* 14 (2022) 465, <https://doi.org/10.3390/polym14030465>.
- [51] D. Herzog, V. Seyda, E. Wycisk, C. Emmelmann, Additive manufacturing of metals, *Acta Mater.* 117 (2016) 371–392, <https://doi.org/10.1016/j.actamat.2016.07.019>.
- [52] Z. Liu, D. Zhao, P. Wang, M. Yan, C. Yang, Z. Chen, J. Lu, Z. Lu, Additive manufacturing of metals: Microstructure evolution and multistage control, *J. Mater. Sci. Technol.* 100 (2022) 224–236, <https://doi.org/10.1016/j.jmst.2021.06.011>.
- [53] S. Jasmee, G. Omar, N.A.B. Masripan, A.A. Kamarolzman, A.S. Ashikin, F.C. Ani, Hydrophobicity performance of polyethylene terephthalate (PET) and thermoplastic polyurethane (TPU) with thermal effect, *Mater. Res. Express* 5 (2018), 096304, <https://doi.org/10.1088/2053-1591/aad81e>.

- [54] K.K. Nielsen, H.N. Bez, L. Von Moos, R. Bjørk, D. Eriksen, C.R.H. Bahl, Direct measurements of the magnetic entropy change, *Rev. Sci. Instrum.* 86 (2015), 103903, <https://doi.org/10.1063/1.4932308>.
- [55] N. Candau, E. Vives, A.I. Fernández, M.L. Maspoch, Elastocaloric effect in vulcanized natural rubber and natural/wastes rubber blends, *Polymer* 236 (2021), 124309, <https://doi.org/10.1016/j.polymer.2021.124309>.
- [56] N. Candau, L. Chazeau, J.M. Chenal, C. Gauthier, J. Ferreira, E. Munch, C. Rochas, Characteristic time of strain induced crystallization of crosslinked natural rubber, *Polymer* 53 (2012) 2540–2543, <https://doi.org/10.1016/j.polymer.2012.04.027>.
- [57] G.A. Holzapfel, J.C. Simo, Entropy elasticity of isotropic rubber-like solids at finite strains, *Comput. Methods Appl. Mech. Eng.* 132 (1996) 17–44, [https://doi.org/10.1016/0045-7825\(96\)01001-8](https://doi.org/10.1016/0045-7825(96)01001-8).
- [58] V.N. Khiêm, M. Itskov, Journal of the mechanics and physics of solids analytical network-averaging of the tube model : strain-induced crystallization in natural rubber, *J. Mech. Phys. Solids* 116 (2018) 350–369, <https://doi.org/10.1016/j.jmps.2018.04.003>.
- [59] C. Koch, L. Van Hulle, N. Rudolph, Investigation of mechanical anisotropy of the fused filament fabrication process via customized tool path generation, *Addit. Manuf.* 16 (2017) 138–145, <https://doi.org/10.1016/j.addma.2017.06.003>.
- [60] A. Nasirov, I. Fidan, Prediction of mechanical properties of fused filament fabricated structures via asymptotic homogenization, *Mech. Mater.* 145 (2020), 103372, <https://doi.org/10.1016/j.mechmat.2020.103372>.
- [61] K.K. Nielsen, K. Engelbrecht, The influence of the solid thermal conductivity on active magnetic regenerators, *J. Phys. D: Appl. Phys.* 45 (2012), 145001, <https://doi.org/10.1088/0022-3727/45/14/145001>.
- [62] K.K. Nielsen, C.R.H. Bahl, A. Smith, K. Engelbrecht, U.L. Olsen, N. Pryds, The influence of non-magnetocaloric properties on the performance in parallel-plate AMRs, *Int. J. Refrig.* 37 (2014) 127–134, <https://doi.org/10.1016/j.ijrefrig.2013.09.022>.
- [63] S. Qian, J. Ling, Y. Hwang, R. Radermacher, I. Takeuchi, Thermodynamics cycle analysis and numerical modeling of thermoelastic cooling systems, *Int. J. Refrig.* 56 (2015) 65–80, <https://doi.org/10.1016/j.ijrefrig.2015.04.001>.
- [64] Y.J. He, Q.P. Sun, Frequency-dependent temperature evolution in NiTi shape memory alloy under cyclic loading, *Smart Mater. Struct.* 19 (2010), <https://doi.org/10.1088/0964-1726/19/11/115014>.
- [65] H. Hou, S. Qian, I. Takeuchi, Materials, physics, and systems for multicaloric cooling, *Nat. Rev. Mater.* 7 (2021) 633–652, <https://doi.org/10.1038/s41578-022-00428-x>.
- [66] J. Tušek, K. Engelbrecht, L.P. Mikkelsen, N. Pryds, Elastocaloric effect of Ni-Ti wire for application in a cooling device, *J. Appl. Phys.* 117 (2015), 124901, <https://doi.org/10.1063/1.4913878>.
- [67] C. Bechtold, C. Chluba, R.L. De Miranda, E. Quandt, High cyclic stability of the elastocaloric effect in sputtered TiNiCu shape memory films, *Appl. Phys. Lett.* 101 (2012), 091903, <https://doi.org/10.1063/1.4748307>.
- [68] L. Mañosa, A. Planes, E. Vives, E. Bonnot, R. Romero, The use of shape-memory alloys for mechanical refrigeration, *Funct. Mater. Lett.* 2 (2009) 73–78, <https://doi.org/10.1142/S1793604709000594>.
- [69] Y. Li, D. Zhao, J. Liu, S. Qian, Z. Li, W. Gan, X. Chen, Energy-efficient elastocaloric cooling by flexibly and reversibly transferring interface in magnetic shape-memory alloys, *ACS Appl. Mater. Interfaces* 10 (2018) 25438–25445, <https://doi.org/10.1021/acsami.8b07703>.
- [70] T.L. Smith, Volume changes and dewetting in glass bead-polyvinyl chloride elastomeric composites under large deformations, *Trans. Soc. Rheol.* 3 (1959) 113–136, <https://doi.org/10.1122/1.548847>.
- [71] G.N. Greaves, A.L. Greer, R.S. Lakes, T. Rouxel, Poisson's ratio and modern materials, *Nat. Mater.* 10 (2011) 823–837, <https://doi.org/10.1038/nmat3134>.
- [72] A. Clausen, F. Wang, J.S. Jensen, O. Sigmund, J.A. Lewis, Topology optimized architectures with programmable Poisson's ratio over large deformations, *Adv. Mater.* 27 (2015) 5523–5527, <https://doi.org/10.1002/adma.201502485>.
- [73] Y.X. Xu, J.Y. Juang, Measurement of nonlinear poisson's ratio of thermoplastic polyurethanes under cyclic softening using 2d digital image correlation, *Polymers* 13 (2021), <https://doi.org/10.3390/polym13091498>.